Evolution of Scalar Fields From Characteristic Data

R. Gómez and J. Winicour

Department of Physics and Astronomy,
University of Pittsburgh,
Pittsburgh, Pennsylvania 15260

and

R. Isaacson

Physics Division, National Science Foundation,
Washington DC 20550

J. Comp. Phys. **98**, 11 (1992).

Abstract

We present a new algorithm for solving nonlinear wave equations when initial data is specified on characteristic surfaces. The algorithm is directly applicable to hyperbolic systems such as Maxwell, Yang-Mills and gravitational fields. The basic principles should also be applicable to hydrodynamics. It is an especially effective approach for studying radiation fields. We show that this method is stable, globally convergent to second order in the grid spacing, and satisfies an energy conservation law. We carry out numerical studies of scalar wave equations with nonlinear self-interactions for some examples of physical interest. We observe nonlinear phenomena such as backscattering, radiative tail decay and approximate analogues to solitons in three-dimensions.

1 Introduction

This paper presents some new numerical techniques for studying radiation problems in hyperbolic physical systems. The physical algorithm underlying these techniques is radically different from the conventional approach which is based upon time evolution of data given at all points of space at the same initial instant of time. Rather it uses concepts developed in the 1960's for studies of gravitational radiation in general relativity [1, 2]. These were prompted by the inability of the major classical tools such as Green's functions and Fourier analysis to overcome the difficulties posed by nonlinearities and gauge freedom.

Such techniques were originally designed for theoretical investigation of the asymptotic behavior of radiation fields. Recently, interest has turned to global questions, and numerical methods based on these algorithms appear to hold much promise as a new tool to investigate these complex problems [3, 4].

This approach is based upon two novel ingredients:

- the dominant role of *characteristic surfaces* and
- the use of *compactification methods* to describe asymptotic properties of radiation.

Characteristic surfaces are the natural tool to use to describe radiation in complex situations. In theoretical analysis it has sometimes been very fruitful to use an initial value scheme which describes time evolution by means of a family of characteristic surfaces. This "characteristic initial value problem" (CIVP) provides a substitute for the familiar Cauchy scheme utilizing a family of successive constant time surfaces to describe dynamical change. For the CIVP, initial data is supplied on a characteristic surface connecting points of space at different times. This approach also demands a completely different form of the mathematical equations and the free initial data.

Compactification methods which provide a rigorous description of asymptotic radiative properties have been based upon characteristic surfaces [2]. The key idea is to introduce a new radial coordinate which ranges over values from 0 to 1 as the actual distance from the source ranges from 0 to ∞. The field equations for the *radiative* field modes are rewritten in terms of these new coordinates. Then, delicate asymptotic questions regarding behavior in the neighborhood of the point at infinity may be studied in terms of the new coordinate which ranges over finite values. In this way, the concept of an *asymptotic limit at infinity* can be given rigorous meaning. Characteristic surfaces are important here since it is in the approach to infinity along these surfaces, not along Cauchy surfaces of constant time, that radiation fields dominate. Even for field equations as complicated as those of General Relativity, this procedure provides not only a rigorous but also an invariant geometrical description of the limit points at infinity reached along characteristic surfaces. Within the literature of relativity, these limit points which form a boundary to the compactified space-time manifold, are referred to as future or past *null infinity* [2]. Here we will use the alternative name *radiative infinity* which seems more appropriate in this context.

There exists a well established methodology for applying characteristics to the study of hyperbolic systems in one space and one time dimension [5]. The advantages of this approach stem from the direct way that characteristics relate a region Ω to its domain of dependence $D(\Omega)$ such that the solution is uniquely determined by initial data in $D(\Omega)$. This leads to the important result that shock fronts only occurs across characteristics. Furthermore, the evolution equations give rise to ordinary differential equations along the characteristics which impose constraints on the propagation of shock discontinuities. Such considerations make it important for the purpose of numerical solution to enforce the propagation along characteristics as extensively as possible.

Waves of amplitude Φ traveling in one spatial dimension with speed c satisfy

$$\frac{1}{c^2}\Phi_{tt} - \Phi_{xx} = 0, \tag{1}$$

where subscripts denote partial derivatives with respect to the independent variables. In this case, there are two characteristics $(x - x_0) = \pm ct$ through each spatial point x_0. In terms of characteristics coordinates $u = ct - x$ and $v = ct + x$, Eq. (1) becomes

$$\Phi_{uv} = 0, \tag{2}$$

with solutions $\Phi = f(u) + g(v)$. Here $g'(v) = \partial_v \Phi$ is the quantity which satisfies the propagation equation

$$\frac{d}{du}\left[g'(v)\right] = 0 \tag{3}$$

along the characteristics in the u-direction. These ideas can be implemented numerically by introducing an (x, t) grid satisfying $\Delta x = c\Delta t$, so that the characteristics pass through diagonal grid points. An exceptional feature of the one-dimensional wave equation is that it can be recast *without error* as a finite difference equation on such a grid. In this simple case, that is the essence of the method of characteristics in one spatial dimension. In practice, the application to numerical solution techniques has been predominantly based upon the conventional Cauchy problem on an (x, t) grid, with initial data $\Phi(x, t_0)$ and $\Phi_t(x, t_0)$ posed at time t_0. This Cauchy data is then propagated to data at time $t_n = t_0 + n\Delta t$ by a finite difference version of characteristic propagation equations such as Eq. (3). Colloquially, this is referred to as "shooting along characteristics".

For hyperbolic systems with two or more spatial dimensions, the manner in which characteristics determine domains of dependence and lead to propagation equations is qualitatively the same. The major difference is that an infinite number of characteristics now pass through each point. In the case of the three-dimensional wave equation,

$$\frac{1}{c^2}\Phi_{tt} - \Phi_{xx} - \Phi_{yy} - \Phi_{zz} = 0\ , \tag{4}$$

the characteristics which pass through the point (x_0, y_0, z_0) at time t_0 are the straight lines which generate the null cone or characteristic cone

$$(x - x_0)^2 + (y - y_0)^2 + (z - z_0)^2 - c^2(t - t_0)^2 = 0. \tag{5}$$

The future (past) null cone consists of the radially outward (inward) characteristics parameterized by $t > t_0$ $(t < t_0)$. There is a 2-parameter set of characteristics through each point corresponding to the sphere of angular directions (θ, ϕ) at that point. This leads to some arbitrariness in formulating an evolution algorithm for Cauchy data based upon shooting along characteristics. There are an infinite number of characteristics and associated propagation equations which can be used to evolve Cauchy data at time t_0 to a point P at time $t_0 + \Delta t$.

For a practical numerical scheme, it is thus necessary either to average these propagation equations appropriately over the sphere of characteristic directions at P or select out some finite number of characteristics whose propagation equations comprise a nonredundant set. The latter approach has been successfully carried out by Butler [6]. For the case of plane flow of an inviscid fluid (a problem in two spatial dimensions), he formulates a shooting algorithm based upon four "preferred" characteristics. In this problem, the geometry is further complicated because the characteristics are dynamically dependent upon the fluid variables, in contrast to the essentially time independent null cones of Eq. (5). In the numerical scheme, the characteristics must themselves be determined by some numerical approximation.

The procedure presented in this paper avoids some of the arbitrariness and awkwardness of Butler's method by using a characteristic initial value approach rather than a Cauchy approach. In order to understand the distinction, it is essential to view space-time as four-dimensional, with initial data given on a three-dimensional hypersurface. More specifically, initial data is now posed on an initial outgoing characteristic cone emanating from the origin, described in terms of some constant u_0 rather than by posing data on a spatial hypersurface $t = t_0$. The evolution then proceeds iteratively to characteristic cones $u_n = u_0 + n\Delta u$. These outgoing characteristic hypersurfaces are intrinsically built into the numerical grid. Furthermore, in evolving from u_n to u_{n+1}, we use an integral version of a shooting algorithm based only upon characteristics which are uniquely and intrinsically picked out by the geometry of the initial data hypersurfaces.

In this paper, we show how these concepts provide the physical basis for a new numerical algorithm. Our aim is to present this approach and to illustrate it with some applications restricted to the case of scalar fields obeying linear and nonlinear wave equations. The nonlinear equations considered here have the simplifying feature that their characteristics have the form of Eq. (5), which is independent of the dynamics of the wave. However, the evolution algorithm which we develop can be taken over intact, except for boundary conditions, to many other hyperbolic physical systems including electromagnetic fields, Yang-Mills gauge fields, as well as to General Relativity in which the characteristics are dynamically dependent. This flexibility is the result of choosing a numerical finite-difference evolution algorithm based upon a form of the evolution equations common to all these systems. All these theories have a common mathematical structure of second order differential hyperbolic equations. Although we have not explored how our approach might be implemented in the case of first order differential hyperbolic systems, such as hydrodynamics, the same general principle should be applicable.

In Section 2 we discuss how a simple identity based upon characteristics can be used to convert the wave equation to an integral equation. This forms the basis for a finite difference scheme presented in Section 3. Numerical results are illustrated in Section 4. To test the algorithm, computed results are compared to known analytic solutions. Questions of convergence and stability are studied both analytically and through numerical tests. Physical results are summarized in Section 5, where consequences of evolution for nonlinear fields are discussed.

2 Theory of the Scalar Wave Equation

2.1 The Characteristic Initial Value Problem

We wish to study the numerical solution of the scalar wave equation (SWE) with appropriate initial data. The SWE is often written in spherical polar coordinates $t, \mathcal{R}, \theta, \phi$ in the form

$$\frac{1}{c^2}\Phi_{tt} = \frac{1}{\mathcal{R}}(\mathcal{R}\Phi)_{\mathcal{R}\mathcal{R}} - \frac{L^2\Phi}{\mathcal{R}^2} \tag{6}$$

$$\mathcal{R} = \sqrt{(x^2+y^2+z^2)}, \tag{7}$$

where c is the wave velocity and L^2 denotes the usual angular momentum operator

$$L^2\Phi = -\frac{(\sin\theta\Phi_\theta)_\theta}{\sin\theta} - \frac{\Phi_{\phi\phi}}{\sin^2\theta}. \tag{8}$$

In our algorithm, we use coordinates $u = ct - \mathcal{R}$, $r = \mathcal{R}$, θ and ϕ. We call u the "retarded time", and $v = ct + \mathcal{R}$ the "advanced time". The outgoing radial characteristics are the curves of constant u, θ and ϕ. These are the curves in the r-direction shown in Fig. 1. In these coordinates, the SWE takes the form

$$2(r\Phi)_{ur} = (r\Phi)_{rr} - \frac{L^2\Phi}{r}. \tag{9}$$

The striking feature about Eq.(9) is that it is only first order in *retarded time* u, unlike the more familiar form of the SWE (6) which is of second order when written in terms of *time* t. When data is given on a characteristic initial hypersurface $u = u_0$, we need only specify the value of the field Φ, and then use Eq. (9) to calculate its retarded time derivative and evolve the initial data. This is in contrast to the conventional Cauchy scheme, where different initial data (the value of Φ and its first *time* derivative) is supplied on the surface $t = t_0$ and Eq. (6) is used to compute the second time derivative so that this data can be evolved to a later value of t.

Numerical solution of the SWE is accomplished by a novel technique. Rather than differencing Eq. (9), this partial differential equation is first converted to an integral equation which is subsequently discretized. The method will be applied to the generalization of the SWE with nonlinear source terms

$$\frac{1}{c^2}\Phi_{tt} = \frac{1}{\mathcal{R}}(\mathcal{R}\Phi)_{\mathcal{R}\mathcal{R}} - \frac{L^2\Phi}{\mathcal{R}^2} + f(\Phi) \tag{10}$$

or, using advanced and retarded time coordinates,

$$4g_{uv} = -\frac{L^2 g}{r^2} + rf(\frac{g}{r}) \tag{11}$$

where $g = r\Phi$.

In the u-r plane formed by fixing the angular coordinates (θ, ϕ), we construct a parallelogram made up of incoming and outgoing radial characteristics which intersect at vertices

P, Q, R, S as depicted in Fig. 1. By integrating Eq. (11) over the area Σ bounded by these vertices, we may establish the identity

$$g_Q = g_P + g_S - g_R + \frac{1}{2}\int_\Sigma dudr\big[-\frac{L^2 g}{r^2} + rf(\frac{g}{r})\big]. \tag{12}$$

This remarkably simple identity is the starting point for the numerical algorithm for time development of the field. It incorporates the essential geometrical role that characteristics play in the SWE.

In order to study the radiative behavior of the field, it is most helpful to transform this equation to new coordinates

$$x = r/(1+r), \quad y = -\cos\theta, \quad 0 \le x \le 1, \quad -1 \le y \le 1. \tag{13}$$

This serves to map an infinite radial domain into a finite coordinate region, and assigns infinitely distant radial points to the edge of the coordinate patch at $x = 1$, denoted as radiative infinity, where the purely radiative fields can be identified. We may convert Eq. (12) into these coordinates by using

$$\begin{aligned} r &= x/(1-x), && (14)\\ L^2 g &= -(1-y^2)g_{yy} + 2y\, g_y - \frac{g_{\phi\phi}}{(1-y^2)}. && (15) \end{aligned}$$

2.2 Energy

The field energy stored in a characteristic hypersurface as well as the power radiated out and escaping to radiative infinity are of paramount physical interest. For nonlinear generalizations of the SWE, such as Eq. (10), solutions are difficult to construct. Conservation of total energy provides an important global check on the behavior of numerical solution when exact solutions are not available.

The energy content of a hypersurface of constant u is given by

$$\begin{aligned} E(u) &= \frac{1}{4\pi}\int_0^{2\pi} d\phi \int_0^{\pi} \sin\theta\, d\theta \int_0^{\infty} r^2 dr\, \{(\Phi_r)^2 + \frac{1}{r^2}(\Phi_\theta)^2 && (16)\\ &\quad + \frac{1}{r^2\sin^2\theta}(\Phi_\phi)^2 + 2V(\Phi)\}\\ &= \frac{1}{8\pi}\int_0^{2\pi} d\phi \int_{-1}^{1} dy \int_0^1 dx\, \Big\{[(1-x)g_x - \frac{g}{x}]^2\\ &\quad + (1-y^2)\frac{(g_y)^2}{x^2} + \frac{(g_\phi)^2}{x^2(1-y)^2} + 2V\Big(\frac{g[1-x]}{x}\Big)\frac{x^2}{(1-x)^4}\Big\} \end{aligned}$$

where the potential $V(\Phi)$ is related to the nonlinear source by $f(\Phi) = -V'(\Phi)$. The power radiated at time u across a spherical surface at constant r is

$$P(u) = \frac{r^2}{4\pi}\int_0^{2\pi} d\phi \int_0^{\pi} \sin\theta\, d\theta\, \Phi_u(\Phi_u - \Phi_r). \tag{17}$$

When the integral is evaluated over the sphere at radiative infinity, the expression above simplifies to

$$P(u) = \frac{1}{8\pi} \int_0^{2\pi} d\phi \int_{-1}^{1} dy (g_u)^2. \tag{18}$$

With these definitions, the field obeys the global conservation law

$$E(u_0) = E(u_1) + \int_{u_0}^{u_1} P(u) du. \tag{19}$$

(This may be derived from the usual application of Gauss' law to a four-dimensional volume bounded by the characteristic hypersurfaces u_0 and u_1 and by radiative infinity.)

Note that the energy density consists of a contribution from the field gradients and one from the potential V but it depends only upon values of Φ on the characteristic cone. This means that we can read off the energy density from a single u-snapshot of Φ, as opposed to a t-snapshot in which the values of Φ_t would contribute.

3 Numerical Algorithm

To develop a discrete evolution algorithm, we work on the set of lattice points

$$\begin{aligned} u_n &= n\Delta u \\ x_i &= i\Delta x \\ y_j &= j\Delta y \\ \phi_k &= k\Delta\phi \end{aligned} \tag{20}$$

and denote the field at these sites by

$$g^n_{ijk} = g(u_n, x_i, y_j, \phi_k). \tag{21}$$

(We will generally suppress the angular indices j and k.)

In choosing a specific parallelogram to rewrite Eq. (12) in the u-x coordinate plane, it is not possible to place the corners P, Q, R and S at coordinate grid points. This is prevented since the slope of the characteristics is not constant in these coordinates, i.e. the coordinate velocity of propagation depends on the location. Detailed numerical experimentation suggests that a stable algorithm with high accuracy will result from the choice made in Fig. 2. The essential feature of this placement of the fundamental parallelogram with respect to a coordinate cell is that the sides formed by incoming characteristics intersect adjacent u-hypersurfaces at equal but opposite x-displacements from the neighboring grid points. This leads to second-order-accurate expressions for coordinates of the vertices

$$\begin{aligned} x_{i-1} - x_P &= x_R - x_{i-1} \\ &= \Delta u(1 - x_{i-1})^2/4 \\ x_i - x_Q &= x_S - x_i \\ &= \Delta u(1 - x_i)^2/4. \end{aligned} \tag{22}$$

The field values at the vertices of the parallelogram are obtained by quadratic interpolation, e.g.

$$g_P = \{g_{i-2}(x_P - x_{i-1})(x_P - x_i) - 2g_{i-1}(x_P - x_{i-2})(x_P - x_i) \\ + g_i(x_P - x_{i-2})(x_P - x_{i-1})\}/(\Delta x)^2. \tag{23}$$

By doing a Taylor series expansion of g around the point at $(x_{i-1/2}, u_{n+1/2})$, it can be seen that

$$g_P = G_P + O((\Delta x)^2), \tag{24}$$

where G represents the exact analytic solution. Cancellations between like terms yields

$$g_Q - g_P = G_Q - G_P + O((\Delta x)^3), \tag{25}$$

$$g_Q - g_P - g_S + g_R = G_Q - G_P - G_S + G_R + O((\Delta x)^3 \Delta u). \tag{26}$$

Note that calculating the expression $g_Q - g_P - g_S + g_R$ to this accuracy is equivalent to computing the second derivative g_{uv} at the point $(x_{i-1/2}, u_{n+1/2})$ to second order.

Now, the integral in Eq. (12) can be evaluated by treating the integrand as a constant over the parallelogram, with value equal to the average at the center. The radial coordinate of the point at the center is calculated as $r_c = (r_P + r_S)/2$. To compute the nonlinear term, the value of g at r_c is taken as the average $g_c = (g_P + g_S)/2$, with g_P and g_S evaluated from second-order linear interpolations over adjacent points on the grid. The angular derivatives in Eq. (12) are replaced with standard second-order-accurate finite difference approximations. $L^2 g$ is calculated on the grid points, and the same interpolation procedure is used to obtain the value of $L^2 g_c$. The integral term is approximated by

$$\int_\Sigma [-L^2 g + r^3 f(g/r)] du\, dr/r^2 = [-L^2 g_c + r_c^3 f(g_c/r_c)] \int_\Sigma du\, dr/r^2 \\ = 2\log(\frac{r_Q r_R}{r_P r_S})[-L^2 g_c + r_c^3 f(\frac{g_c}{r_c})] \; . \tag{27}$$

Note that in the above procedure we carried all interpolations and derivatives to second order, hence the integrand is accurate to second order in Δx and Δy. The result of these substitutions gives the final finite difference equation

$$\begin{aligned} & g_i^{n+1}(x_Q + x_P - x_{i-2} - x_{i-1}) = \\ & \quad 2g_{i-1}^{n+1}(x_Q + x_P - x_{i-2} - x_i) - g_{i-2}^{n+1}(x_Q + x_P - x_{i-1} - x_i) \\ & \quad + \{g_{i+1}^n(x_S + x_R - x_{i-1} - x_i) - 2g_i^n(x_S + x_R - x_{i-1} - x_{i+1}) \\ & \quad + g_{i-1}^n(x_S + x_R - x_i - x_{i+1})\}\frac{(x_S - x_R)}{(x_Q - x_P)} \\ & \quad + \int_\Sigma \frac{dr du}{r^2}\Big[-L^2(g_c) + r_c^3 f(\frac{g_c}{r_c})\Big]\frac{(\Delta x)^2}{(x_Q - x_P)}. \end{aligned} \tag{28}$$

Eq. (28) connects values of g_i^{n+1} with those of neighboring points on the coordinate lattice which are either earlier in time $(g_{i-1}^n, g_i^n, g_{i+1}^n)$, or else contemporary but located at smaller radius $(g_{i-2}^{n+1}, g_{i-1}^{n+1})$. Consequently, it is possible to move through the interior of the lattice, computing g_i^{n+1} explicitly by an orderly march. This is achieved by starting at the origin at time u_{n+1}. Field values vanish there. Proceed outward one radial step using the boundary conditions discussed below. Repeat for all angular sites on the lattice. Step outward to the next interior radial point, apply Eq. (28) for all angles, and iterate this process throughout the interior. Thus, all the field values out to radiative infinity along the new characteristic cone at u_{n+1} are updated, completing one evolutionary time step.

To completely specify the evolution algorithm we need to describe the treatment of $g(u, x, y, \phi)$ at the coordinate boundaries. Initial data is given at $u = u_0$ to start the method. Periodic boundary conditions are applied for the angle ϕ, so that $g(u, x, y, 0) = g(u, x, y, 2\pi)$. Angular derivatives at the axis $y = \pm 1$ are computed using second-order-accurate forward or backward differences. At the radial edges of the coordinate grid at the origin and radiative infinity, Eq. (28) no longer applies, and it is necessary to reapply the basic integral identity Eq. (12). This is done in a straightforward fashion; g vanishes at $x = 0$ so that $g_0^{n+1} = 0$ whereas at radiative infinity the points Q and S are grid points so that $x_P = x_S = 1$.

4 Testing the Numerical Code

In this section, we will test the new theoretical approach just introduced with some numerical test problems. For simplicity, we will restrict attention to the evolution of fields with both axial symmetry and reflection symmetry across the equatorial plane (i.e., g is an even function in y).

To better understand the *stability* of the explicit algorithm, we consider the geometrical constraints imposed by the Courant-Friedrichs-Lewy (CFL) condition. This requires that the analytic domain of dependence for the equation be contained in the numerical domain of dependence. This will be satisfied if each grid point at u_n appearing in Eq. (28) lies on or outside of the past characteristic cone of the point $(x_i, y_j, \phi_k, u_{n+1})$ to which the field is being evolved.

In coordinates $x^\alpha = (t, x, y, z)$, the condition that two points p and q lie on a characteristic is, according to Eq. (5),

$$(x_q - x_p)^2 + (y_q - y_p)^2 + (z_q - z_p)^2 - (t_q - t_p)^2 = 0. \tag{29}$$

We want to express this condition in radial coordinates, but since we are interested here in problems with axial symmetry, it suffices to consider points at $\phi = 0$. Then two points p and q, with coordinates

$$\begin{aligned} p^\alpha &= (\Delta u, r, \theta, 0), \\ q^\alpha &= (0, r - \Delta r, \theta + \Delta\theta, 0), \end{aligned} \tag{30}$$

will lie along a characteristic if and only if

$$\begin{aligned} &(\Delta u + \Delta r)^2 - (r \sin\theta - (r - \Delta r)\sin(\theta + \Delta\theta))^2 \\ &\qquad -(r\cos\theta - (r - \Delta r)\cos(\theta + \Delta\theta))^2 = 0. \end{aligned} \tag{31}$$

For p in the future of q, the solution is

$$\frac{\Delta u}{\Delta r} = -1 + \sqrt{K^2 + (K-1)^2 - 2K(K-1)\cos\Delta\theta}, \tag{32}$$

where $K = r/\Delta r$. For fixed r, the smallest allowed value of Δu occurs at the equator, where $\theta = \frac{\pi}{2}$, and $\Delta\theta = \Delta y$. This can be re-expressed in terms of the x-coordinate of the point p using

$$\Delta r = r_p - r_q = \Delta x \frac{1 - 2x_p}{(1-x_p)(1-x_p-\Delta x)}, \tag{33}$$

so that

$$K = \frac{x_p(1-x_p-\Delta x)}{\Delta x(1-2x_p)}, \tag{34}$$

and

$$\frac{\Delta u}{\Delta x} = (\sqrt{1 + 2K(K-1)(1-\cos\Delta y)} - 1) \times \frac{(1-x_p)(1-x_p-\Delta x)}{(1-2x_p)}. \tag{35}$$

Equation (35) determines the maximum allowable retarded time step Δu in terms of the grid spacings Δx and Δy. The maximum time step increases with increasing values of x_p and it is approximately inversely proportional to the square of the number of angular points. For grid points sufficiently close to the origin, we can approximate Eq. (35) by

$$\Delta u \approx K\Delta x(\Delta y)^2 \tag{36}$$

where the coefficient K is given by

$$K = I(I-1)/2 \tag{37}$$

and the index I labels the innermost site on the numerical lattice where the algorithm is applied. The final stability picture is complicated by the fact that a different scheme is used to evolve the origin and the first radial point ($i = 0, 1$) where special boundary and start-up conditions are used (see the last paragraph of Sec. 3). These points also feed into the numerical algorithm for $i = 2, 3$. Thus, the first truly independent use of the algorithm occurs when $i = 4$.

Consequently, we should expect stable propagation for time steps satisfying Eq. (36) with I in the range $2 \leq I \leq 4$. For initial data given by

$$g(0, r, y) = \frac{8(4r^3y^2 + 2r + 1)}{(1+2r)^3}. \tag{38}$$

and for a fixed $(\Delta x)^{-1} = 99$, numerical stability tests verify the validity of this estimate with $I = 3.4$, as indicated in Table I.

TABLE I

Stability coefficient K as a function of the step size Δy

$(\Delta y)^{-1}$	$K(Stable)$	$K(Unstable)$
14	4.1	4.3
19	3.9	4.3
24	4.0	4.6
29	4.0	4.2
34	4.0	4.2

This situation is in contrast to the stability requirements for normal Cauchy evolution where application of the CFL condition leads to the analogous requirement that

$$\Delta t \le \sqrt{2}\, I \Delta x \Delta y. \tag{39}$$

The extra power of Δy in Eq. (36) is the penalty paid for the overall simplicity of the characteristic method. Nevertheless, the CIVP approach offers offsetting advantages, especially for applications to multicomponent fields such as those of general relativity.

With stability explored, we turn next to study the question of global convergence. Here, we introduce as a measure of error the ℓ_∞ norm of the difference between g, the numerical solution, and G, the exact analytic solution, i.e.

$$||g - G||_\infty = \max |(g^n_{ijk} - G^n_{ijk})| \tag{40}$$

where n, i, j and k range over all lattice sites.

The following three global exact solutions of the SWE represent fields of different pure multipole moments l in terms of Legendre polynomials $P_l(y)$:

$$G^{(l)}(u,r,y) = \frac{r^{l+1} P_l(y)}{(u+1)^{l+1}(u+2r+1)^{l+1}}, \quad l = 2,4,6\,. \tag{41}$$

These solutions represent waves which are regular for $u > -1$. They provide comparison data for a family of corresponding numerical solutions which are run on a series of different grid sizes for $u > 0$. Fig. 3 shows the global error as a function of grid size Δx (while Δy and Δu are kept at fixed ratio to Δx). The log-log plots approach slope 2 for small Δx, as is expected for a second-order-accurate method.

As a test problem, we examine the case of the nonlinear SWE Eq. (10) with $f(\Phi) = -k\Phi^3$, so that $V(\Phi) = \frac{1}{4}k\Phi^4$. This equation has attracted considerable interest as a model for a conformally invariant quantum field theory (the so-called "Φ^4" theory [7], see also [8, 9]). It is of special interest since Φ^4 is the lowest order monomial potential which allows $O(1/r)$ radiation fields.

We have found an exact axisymmetric solution, with t and y reflection symmetry given by

$$\Phi = 2\Big\{\frac{2a}{8akr^2y^2 + [u(u+2r) + 2ak^2]^2}\Big\}^{1/2}. \tag{42}$$

This solution has singularities in the equatorial plane ($y = 0$) on the hyperbolae $t^2 - r^2 = -2a^2k$. For negative k, the singular hyperbolae will be spacelike, and this solution will be regular between them for u in the range $-(2k)^{1/2}a < u < +(2k)^{1/2}a$. Within this range, we can test our nonlinear code and check its behavior in the approach to a singularity. Detailed tests again confirm global second-order convergence using the ℓ_∞ norm.

For this exact solution, the energy is given by

$$E(u) = \frac{a[\mathrm{atan}(m/u)(u^2 - 3m^2)(u^2 + m^2) - mu(u^2 + 3m^2)]}{4m^3u^2(u^2 + m^2)}, \tag{43}$$

where $m = (2ak)^{1/2}$. This allows detailed numerical checks on the energy, as well as on the global energy conservation during evolution. Using a grid of 65 radial and 33 angular points, numerical solution for the case $a = 1/2, k = 1$ was carried out from different initial surfaces. Near the singularity, starting from $u_0 = 0.1$ the amplitude of the solution decays by an order of magnitude as it evolves to $u_1 = 0.2$. This limits overall numerical accuracy for the field at the end to 1%, and conservation of energy holds at the same level. For evolution of the same time duration between $u_0 = 1.0$ to $u_1 = 1.1$, far from the singularities, conservation of energy is verified to better than .01%.

5 Discussion of Numerical Evolution Results

We shall now illustrate the effectiveness of the code in revealing new physical features of nonlinear scalar waves, especially those that are intrinsically related to characteristic hypersurfaces and to radiative infinity. We wish to emphasize that many of these phenomena, which can be described in a natural way in terms of our algorithm, would be difficult or impossible to extract in conventional numerical approaches.

Using some examples of numerical solution, we shall discuss the generic effects of nonlinearities on propagation, backscattering, and radiative tails. We also explore different nonlinear potentials to get a feeling for the consequences of specific aspects of the potential such as saturation and degenerate minima.

It is important to establish some effective basis for revealing those qualitative properties generic to fields evolving under the action of different nonlinear potentials. We accomplish this here by choosing common initial data for all our examples. We restrict our attention to spherically symmetric cases. While we have made samples of angular dependent nonlinear evolution, these lead to more complex behavior obscuring simple physical insights. It is not our purpose to treat such details here. Furthermore, in order to isolate those features intrinsic to the data from those intrinsic to the evolution, we choose very simple initial data having the form of a (rounded) step function for $\Phi(u_0, r)$. This corresponds to a (rounded) sawtooth shape for $g(u_0, r)$ as shown in Figs. 4 and 5. (The rounding is implemented by third order polynomials.) The discussion will, at first, be expressed in terms of displays of $g(u, x)$ for differing potentials V. Later, we will discuss features which only become prominent when expressed in terms of Φ.

5.1 Tails

As is well known, Huyghen's principle applies to a few special systems such as the linear wave equation in an odd number of spatial dimensions. For such systems, radiation propagates outwards along the forward characteristic cone and does not leak into its interior. For more general hyperbolic systems, such as Eq. (10), radiation backscatters energy into the interior while traveling on an outward characteristic cone. Even when the initial field has compact support, this leaves behind a radiative tail which survives over long time scales. This field is typically small, and dies off as multiple backscatterings dissipate its energy in radiation.

The slope of g at radiative infinity (on a $g(x)$ versus x graph) is a dynamical quantity of particular relevance for the development of tails. It is conserved for the linear wave equation and for potentials of higher than fourth order in Φ. (It is a special case of a general class of asymptotic quantities that are conserved for fields which are suitably linear at radiative infinity [10].)

This quantity, corresponding to the monopole term in the $O(1/r^2)$ part of Φ, is not, however, conserved for the Φ^4 theory. We may see this by expanding g as

$$g = \sum_{n,l,m} \frac{a_{nlm}(u) Y_{lm}(\theta, \phi)}{r^n} \tag{44}$$

and substituting this into Eq. (10). For a potential of order p, this gives

$$2g_{ur} = g_{rr} - \frac{L^2 g}{r^2} - \frac{k g^p}{r^{p-1}}. \tag{45}$$

For $p = 3$, corresponding to Φ^4 fields, this leads to the relation

$$\frac{d}{du} a_{100} = (k/2) a_{000}^3. \tag{46}$$

First, suppose that the nonlinear coupling is turned off ($k = 0$), so that a_{100} is a constant. Then if the initial data has compact support, this constant is initially zero and must remain zero. On the other hand, the conservation law implies that linear fields, with initial data for which $a_{100} \neq 0$, cannot evolve to zero in any finite retarded time. As an example consider the field $\Phi = (u(u+2r))^{-1}$, a solution of Eq. (9) in the future of the coordinate origin. For this field,

$$g = \frac{x}{u[2x + u(1-x)]}. \tag{47}$$

At radiative infinity ($x = 1$), $g_x = 1/4$ which leads to the radiative tail $g(u,1) = 1/(2u)$. The code successfully tracks this conservation law until the field localizes into the last few grid cells before $x = 1$, as shown by the numerical runs plotted in Fig. 6. In the nonlinear case of Φ^4 fields, even if the initial data were compact, a_{100} would not vanish during the early stage of nonlinear radiation. Then, when the nonlinear field dissipates into the linear regime of Eq. (9), it is left with a nonvanishing a_{100} which results in a $1/u$ radiative tail.

5.2 Linear Waves ($V = O$)

The evolution of Φ, for an initial pulse with $g = r\Phi$ having a sawtooth profile, is displayed in Fig. 7 and the accompanying radiation in Fig. 8. Here g satisfies the one-dimensional wave equation. Pulse-like data on an initial outgoing characteristic cone corresponds to an initial state consisting of purely incoming radiation. The sawtooth travels toward the origin with speed $\Delta r/\Delta u = 1/2$, moving in analogy with a pulse on a string traveling toward a perfectly reflecting barrier. However, in this case, as the pulse hits the origin it is immediately transported to infinity in terms of the characteristic coordinate u. Also, note that the velocity of propagation is not constant with respect to the x-coordinate so that some alteration in pulse shape appears in the figures. Because of the phase reflection, the instantaneous radiation produced by the leading part of the pulse superimposes destructively with the trailing part.

Initially the radiation power is constant, in accord with the linear r dependence of the leading edge, and the total energy in the pulse decreases linearly in time. It is a very useful feature of retarded coordinate system that the energy density Eq. (16) can be read off from an instantaneous u-snapshot of the pulse. For $V = 0$, it is proportional to $(d\Phi/dr)^2$ so that it is concentrated in the trailing edge of the pulse. When this edge hits the origin there is a large burst of radiation which carries away the remaining energy in the system.

As expected, no field remains after one crossing time (the time it takes the outer edge of the pulse to propagate to the center). The entire evolution is strictly governed by propagation effects with no other underlying story of physical interest. There is no tail to the radiation and the slope of $g(x)$ at radiative infinity remains zero throughout the evolution in accord with the conservation discussed in Sec. 5.1.

5.3 Strongly Nonlinear Potential ($V = k\Phi^4$)

For this potential, the effect of the nonlinearities grows with increasing Φ. The initial data starts in a strong field configuration and so probes precisely this important case. The time development for the standard sawtooth initial data is radically changed from the previous example, and proceeds along a markedly different course. This is shown in Fig. 9 and Fig. 10 (In all numerical runs we set $k = 1$).

The initial energy of the system from Eq. (16) is now totally dominated by the self-interaction term in the potential which far outweighs the field gradients. Consequently, the energy stored in the initial data is almost a factor of twenty higher than for the linear case corresponding to vanishing potential.

As the initial sawtooth starts its development, the strong nonlinear potential acts to backscatter the wave, immediately repelling any inward propagation onto the outgoing characteristic cone. By the very first time step, a violent burst of radiation reaches radiative infinity, carrying off about 80% of the large initial energy. This depletes the strength of the remaining field and so effectively turns down the strength of the self-interaction, reducing the backscattering. Consequently, the remaining field enters a quasilinear regime and resumes the inward propagation associated with a linear field. Then, it is only able to carry off the bulk of the remaining energy after one crossing time.

However, the imprint of the nonlinear potential still remains observable in the fine details of the tail to the radiation at radiative infinity. After long times, g still persists there. In Fig. 11 the behavior of this remnant amplitude decreases as $1/u$, just as expected from the considerations of Sec. 5.1. This figure also shows the change of the slope of $g(x)$ at radiative infinity due to the non-conservation also discussed in that section. In the quasilinear regime, this change progresses more and more slowly with time. Theoretical analysis indicates that the slope approaches a constant value as $1/u^2$, in agreement with the numerical behavior.

In (t, r) coordinates, a field satisfying $\Phi_r = 0$ will undergo a periodic oscillation in any potential with a minimum. For an initially large amplitude in a Φ^4 potential, this would introduce a rapid oscillation leading quickly to a sign reversal in Φ. In the present case, one might have expected the field to undergo such a sign reversal in the inner region where the initial data is constant. However, in terms of (u, r) coordinates, the situation is quite different. The condition $\Phi = \Phi(t)$ becomes $\Phi_u - \Phi_r = 0$ which leads, via the wave equation Eq. (11), to the equation for a particle in a potential,

$$\frac{\partial^2 \Phi}{\partial r^2} = -V'(\Phi). \tag{48}$$

In (u, r) coordinates, a purely t-periodic Φ would have to satisfy Eq. (48) on an outgoing characteristic cone. In fact, the field in the inner region with characteristic data $\Phi = constant$ does not undergo a sign reversal but gently settles to zero, as is evident in the numerical solution displayed in Fig. 12. There is a purely analytic explanation of this behavior in terms of the exact solution

$$\Phi = \frac{a}{u(u+2r) + \frac{k}{2}a^2}, \tag{49}$$

where a is a free parameter. Evaluation of this solution (49) on the hypersurface $u_0 = 0$ induces characteristic data $\Phi = const.$ Evolution of such data therefore leads to the monotonic asymptotic decay described by (49).

One outstanding feature, which develops in Fig. 9 on the scale of the crossing time, is the reconstruction of a somewhat attenuated and distorted version of the initial data. This is apparently an effect of backscattering but we do not understand the details of the underlying mechanism.

5.4 Saturated Nonlinear Potential ($V = ksin^4(\Phi)$)

In this case, since there are no known exact solutions, numerical simulations were performed with successive mesh refinement until there were no discernible differences in wave forms. Concomitantly, energy was conserved to high precision.

For $\Phi \ll \pi$, this potential behaves much as the Φ^4 model in the quasilinear regime. As Φ increases into the nonlinear regime, the potential exhibits a succession of degenerate minima and maxima, which leads to trapping effects, but remains bounded in value, which leads to saturation effects. The initial data starts the field off in the first minimum of the potential as the sawtooth in $g(x)$ ramps up. Past the edge of the tooth, the field is in the vacuum state, degenerate in potential energy with the first minimum. At the edge of the sawtooth, a transition region connects the two minima. Only in this region does the field have any energy density, arising here from both field gradient and potential. Because of the small extent of this region and the falling value of the potential there, the total energy is only about 10% higher than in the linear case. This initial configuration and nonlinear field equation correspond to a bubble surrounded by a domain wall of the sort that has been of some recent interest to studies of the early universe.

The evolution of this system is shown in Figs. 13 and 14. The saturation of the potential vitiates the effects of backscattering, and so there is no large initial surge of outgoing radiation. The field propagates toward the origin, and, after one crossing time, emits a pulse of radiation as the tooth edge hits the origin. This carries off about one third of the total energy of the system in terms of radiation. After another crossing time, the remaining energy is redistributed in a configuration similar to the initial kink. Then, the field recollapses toward the origin, and after another crossing time again emits a pulse of radiation, removing about as much energy as the first pulse. At this stage, the system is quasilinear. As in the Φ^4 case, backscattering of the initial radiation pulse leads to several rough reconstructions of the initial energy distribution as shown in Fig. 15. Experimentation with other potentials indicates that this is an important generic effect. Unfortunately, we have not found analytic means of investigating this phenomenon.

A striking feature of the solution is the formation of a long-lived node, at which Φ_u vanishes, occurring at about the same time that the kink reforms. At $u = 7.6$, the field at the point $x = .6$ settles on a minimum of the potential (at $\Phi = \pi$). As displayed in Fig. 16, the value of the field at this point remains constant between $u = 7.6$ and $u = 9.1$. During this interval, energy flows into the neighborhood of this node from both the inner and outer directions. Initially the slope of Φ at the node is zero, but as energy accumulates, the slope gradually increases. Finally, the kinetic energy reflected in the increasing slope of Φ lifts the field out of the potential well, and the configuration propagates inward. This example again illustrates the underlying influence of one-dimensional solitary wave phenomena, which in some approximate sense take place also in the three-dimensional case.

6 Conclusion

In this work, we have developed an algorithm for the numerical solution of nonlinear wave equations which implements the CIVP approach on characteristic cones. The physical reasons to favor this approach over the more common Cauchy problem were outlined in Section 1. We have shown that this algorithm is stable, subject to the CFL condition. We have tested the algorithm against exact nonlinear solutions and have shown that the numerical solution is globally convergent to second order in the grid spacing. Although we have not extensively investigated the effects of numerical dispersion in our approach, its effects did not seem important even in test cases with initial data containing large spatial gradients. Numerical tests on various models also demonstrate that the algorithm is conservative, in the sense that it accurately satisfies energy conservation.

In the next stage, we have used our code to study nonlinear systems of physical interest, such as self-interacting fields with Φ^4 and $sin^4\Phi$ potentials. In this process, the algorithm proved effective in revealing nonlinear phenomena, such as backscattering, the formation of kink-like configurations, node formation and radiative tail decay. Our studies show that it is numerically possible to implement compactification techniques to treat radiation at radiative infinity in a CIVP approach. Tests made with Φ^4 fields indicate that the CIVP can also be used to study singularity formation.

The physically simplistic models discussed here were chosen more to illustrate methodology and mathematical issues than to represent actual phenomena. In a more realistic application, a key aspect of the problem would be the selection of initial characteristic data to represent properly the source of the wave disturbance. This is no different, in principle, than the initial data problem in the more familiar Cauchy approach, where there exists much experience and physical intuition to serve as guide. Two types of generic situation exist.

In the first, the system is excited by incoming waves. An initially linear wave will focus in intensity so that nonlinear effects will become important. The goal is to study these nonlinear effects numerically. The initial data problem is to specify the waveform at some initial time when the system is still linear. One way to induce characteristic data is by evolving Cauchy data forward in time to a characteristic cone by treating the linear case analytically.

In the second situation, the system is excited by an external source which drives the wave equation. This would be incorporated into the characteristic evolution algorithm as an additional term in the integral equation Eq. (12). A corresponding procedure would be implemented in the Cauchy approach. A typical example is a sound wave emanating from an explosion. The initial condition is that there be no incoming waves. The characteristic initial data and the Cauchy data would be set to zero just prior to the explosion. Waves would arise as a result of the driving term. For this case, the procedure for formulating the two initial value problems is similar, although the characteristic version more efficiently avoids the wave-free points of space-time.

The basic algorithm is directly applicable to other hyperbolic systems such as Maxwell, Yang-Mills and gravitational fields. The additional step necessary here is to numerically integrate some radial differential equations which intermediate the evolution equations on each characteristic cone. Our primary motivation is the solution of the field equations of general relativity, for which numerical solutions of these characteristic cone equations are already available [3]. However, we also wish to encourage application of this approach to hydrodynamical problems.

7 Acknowledgements

We would like to express our thanks to the National Center for Supercomputing Applications and the Pittsburgh Supercomputing Center for making computing time available for this research. We would also like to thank the referees for suggesting changes intended to make this paper readable by a wider audience. RG and JW would like to thank the National Science Foundation for research support under NSF grant PHY-8803073.

References

[1] H. Bondi, M.G. van der Burg, and A.W.K. Metzner, *Proc. R. Soc. London Ser.*

A 270, 103 (1962).

[2] R. Penrose, *Phys. Rev. Lett.* **10**(2), 66 (1963).

[3] R.A. Isaacson, J.S. Welling, and J. Winicour, *J. Math. Phys.* **24**(7), 1824 (1985).

[4] R. Gómez, R. A. Isaacson, J. S. Welling, and J. Winicour, in *Dynamical Spacetimes and Numerical Relativity, Philadelphia, 1985*, edited by Joan M. Centrella (Cambridge University Press, Cambridge, 1986), p. 236.

[5] F. John *Partial Differential Equations*, Springer-Verlag (New York, Berlin), Fourth Edition, (1982).

[6] D. S. Butler *Proc. R. Soc. London Ser.* **A 255**, 232 (1960).

[7] L. Castell *Phys. Rev. D* **6**, 536 (1972).

[8] G. B. Whitham *Linear and nonlinear waves*, Wiley (New York), (1974)

[9] R. Rajaraman, *Phys. Rep* **21C**, 227 (1975).

[10] E. T. Newman and R. Penrose, *Proc. R. Soc. London Ser.* **A 305**, 175 (1968).

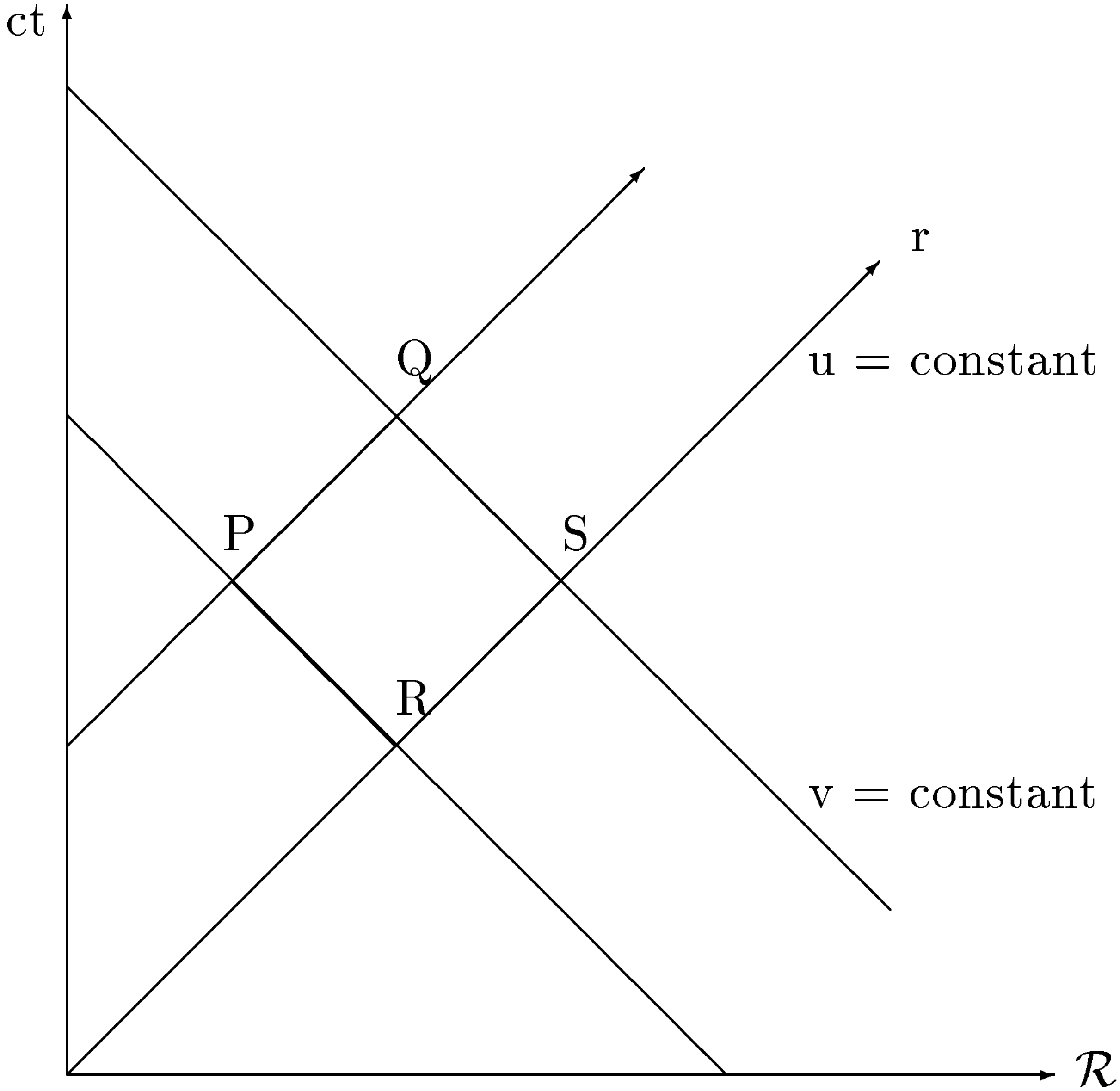

Figure 1: Line segments drawn at forty-five degrees to the vertical represent radial characteristics. Their intersection defines the fundamental parallelogram PQRS which is used in our numerical method.

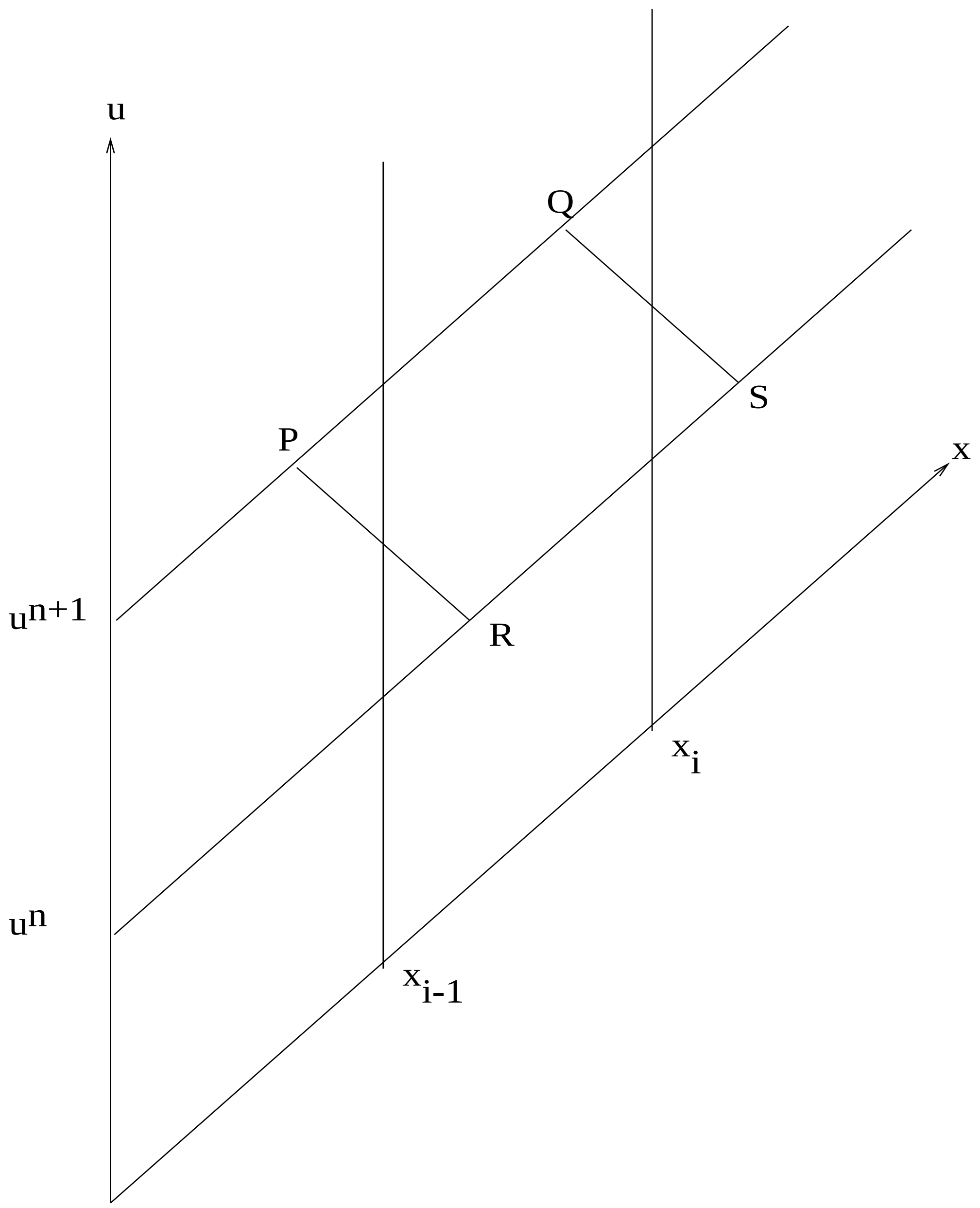

Figure 2: The same fundamental characteristic parallelogram PQRS which was geometrically defined in Figure 1 is now displayed superimposed upon the new (x, u) coordinates. Note that the parallelogram no longer falls on the coordinate grid.

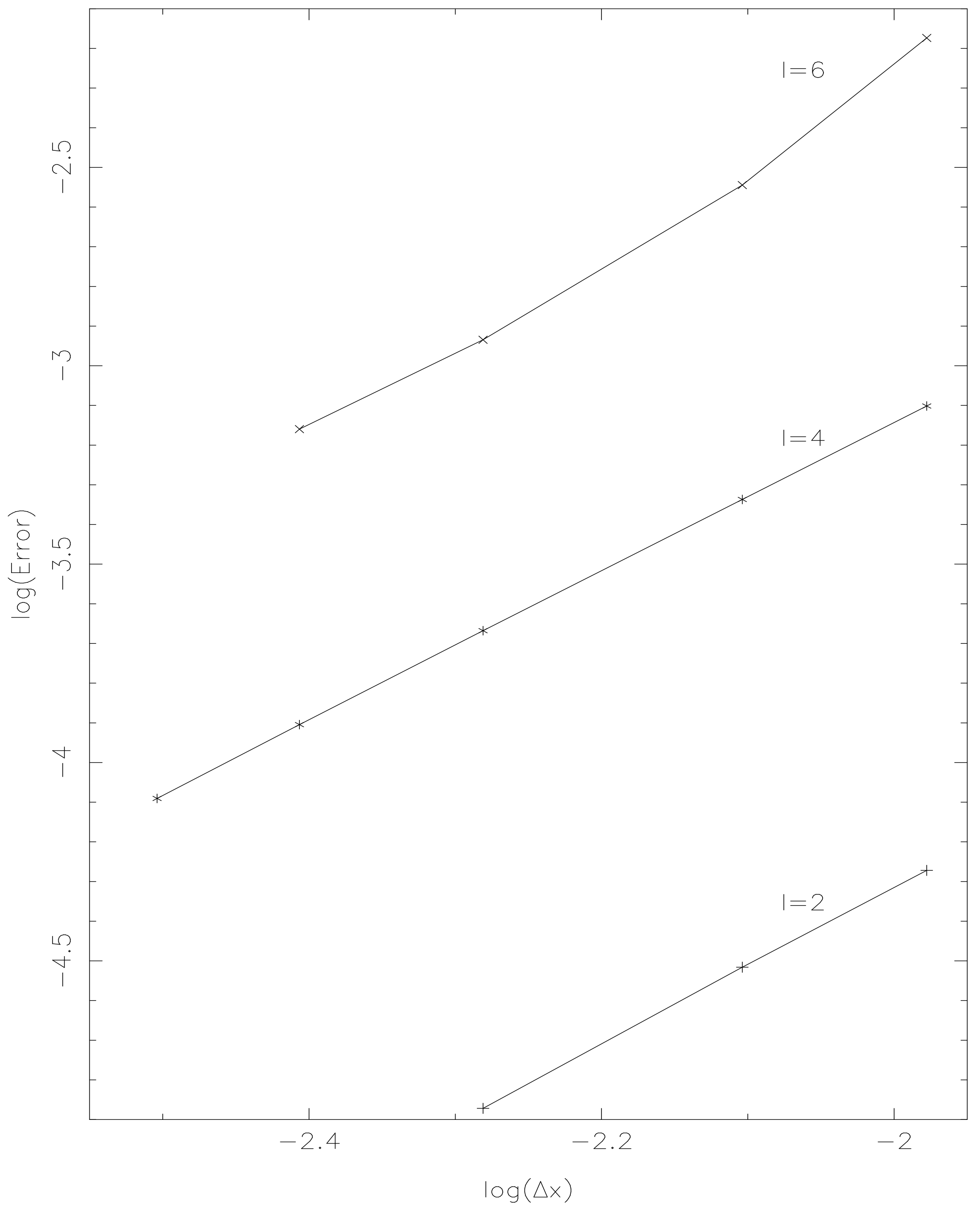

Figure 3: The convergence of the numerical to the exact solution is shown for pure multipole initial data for the vacuum scalar wave equation. The error is measured by the ℓ_∞ norm. Lines connect points corresponding to the same multipole and different grid spacing.

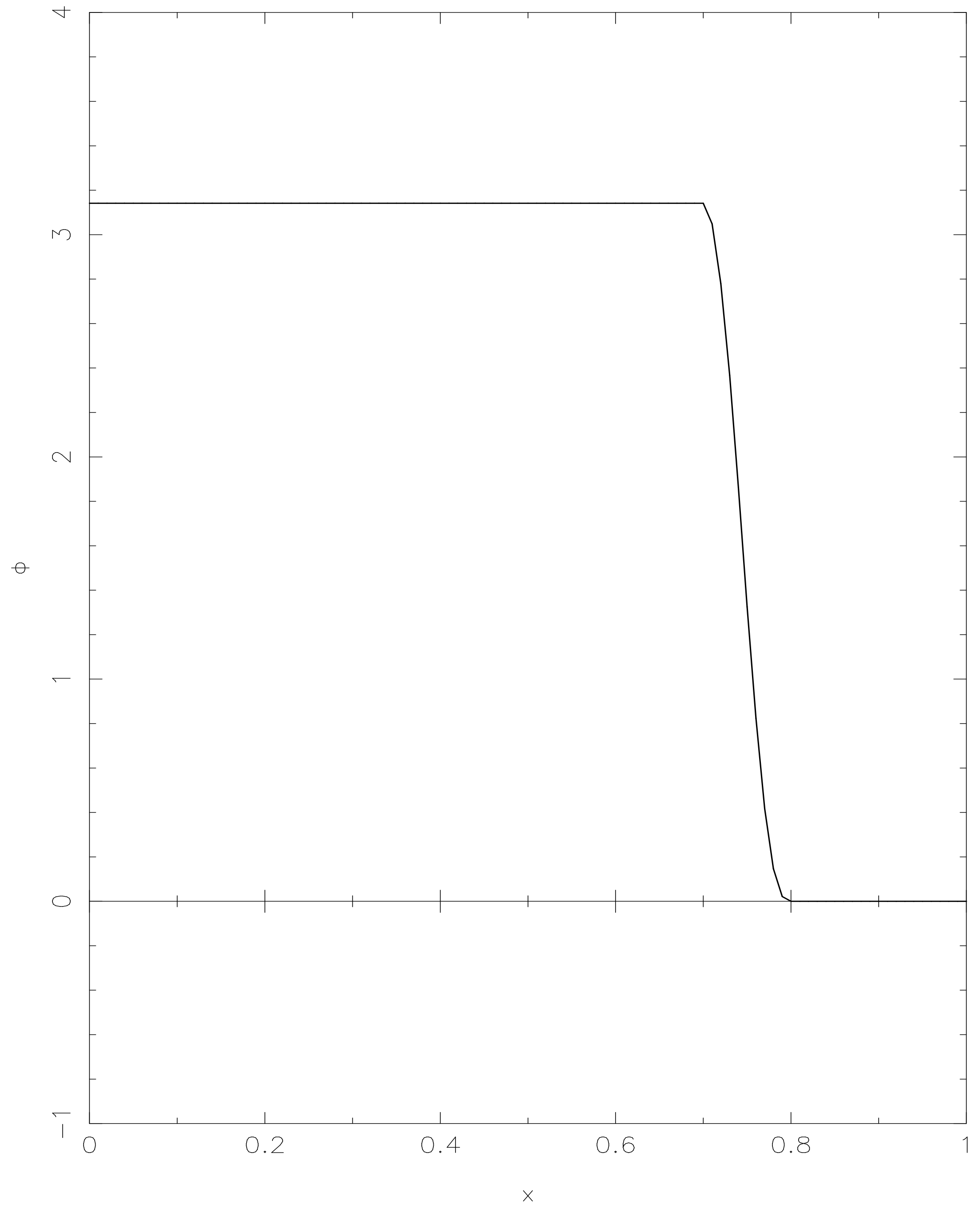

Figure 4: Initial data for $\Phi(u_0, x)$ used to compare the qualitative behavior of different potentials.

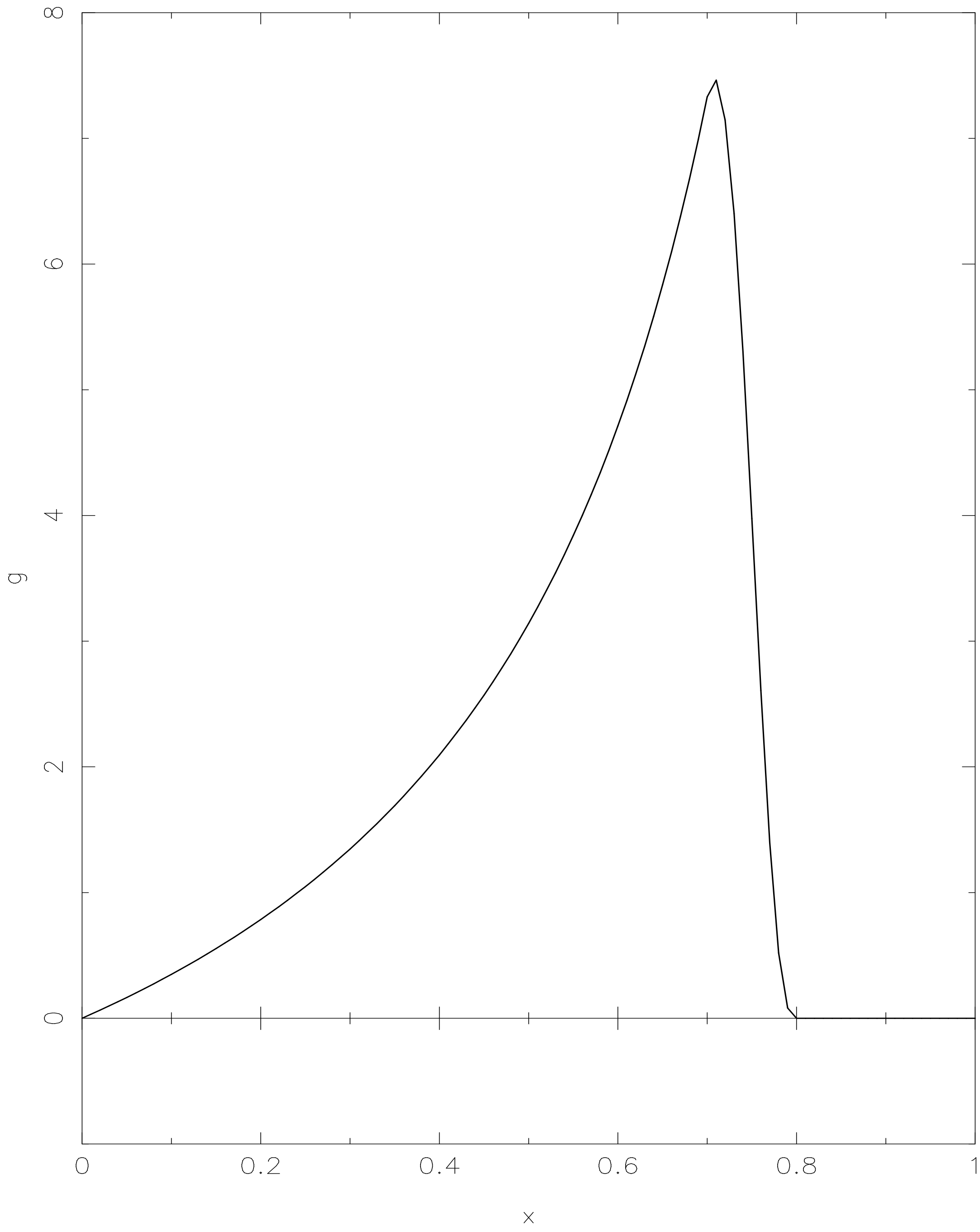

Figure 5: Initial data for $g(u_0, x)$ used to compare the qualitative behavior of different potentials.

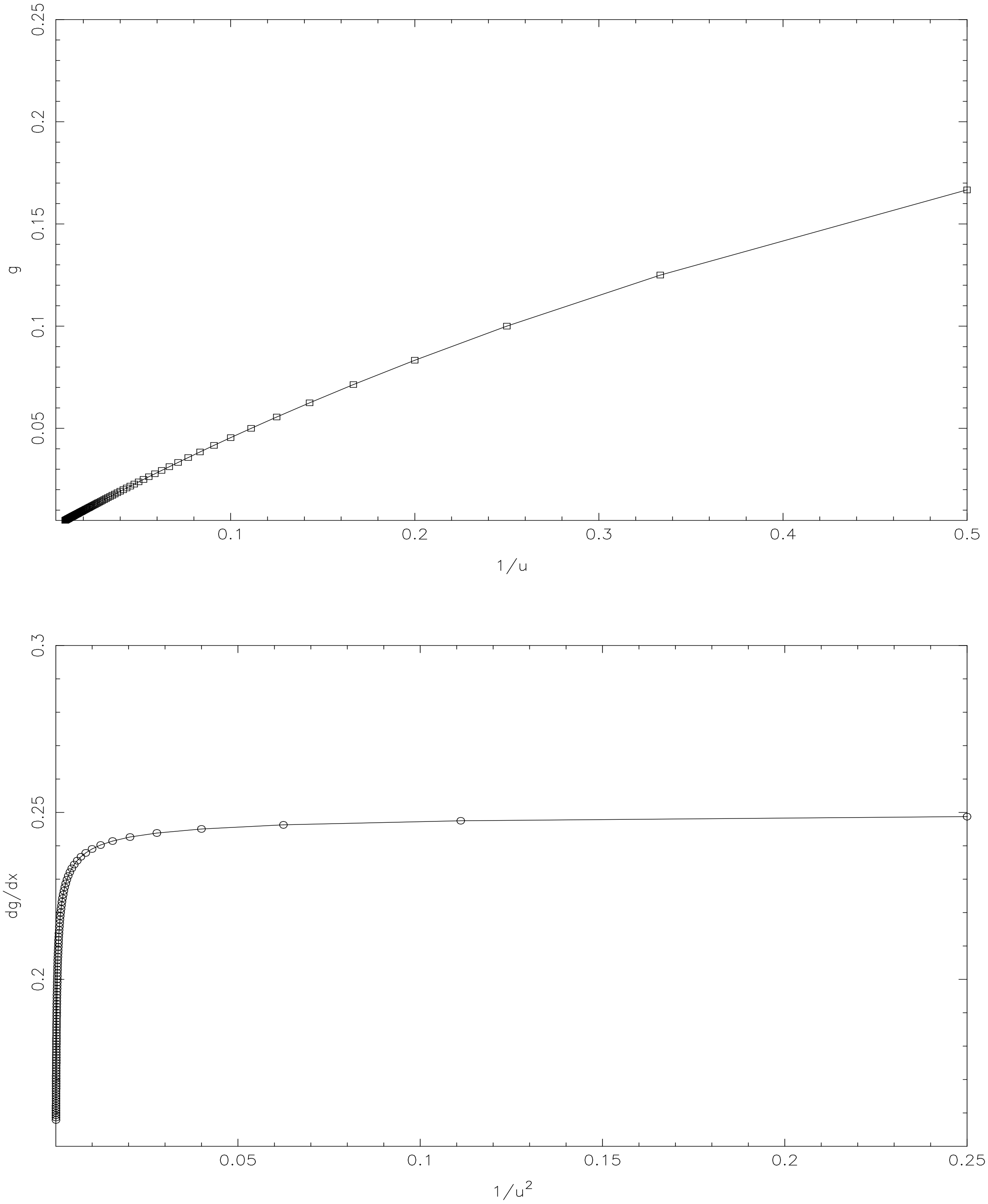

Figure 6: The time dependence of radiative tails for scalar waves propagating in vacuum is illustrated by the behavior of g and g_x at radiative infinity.

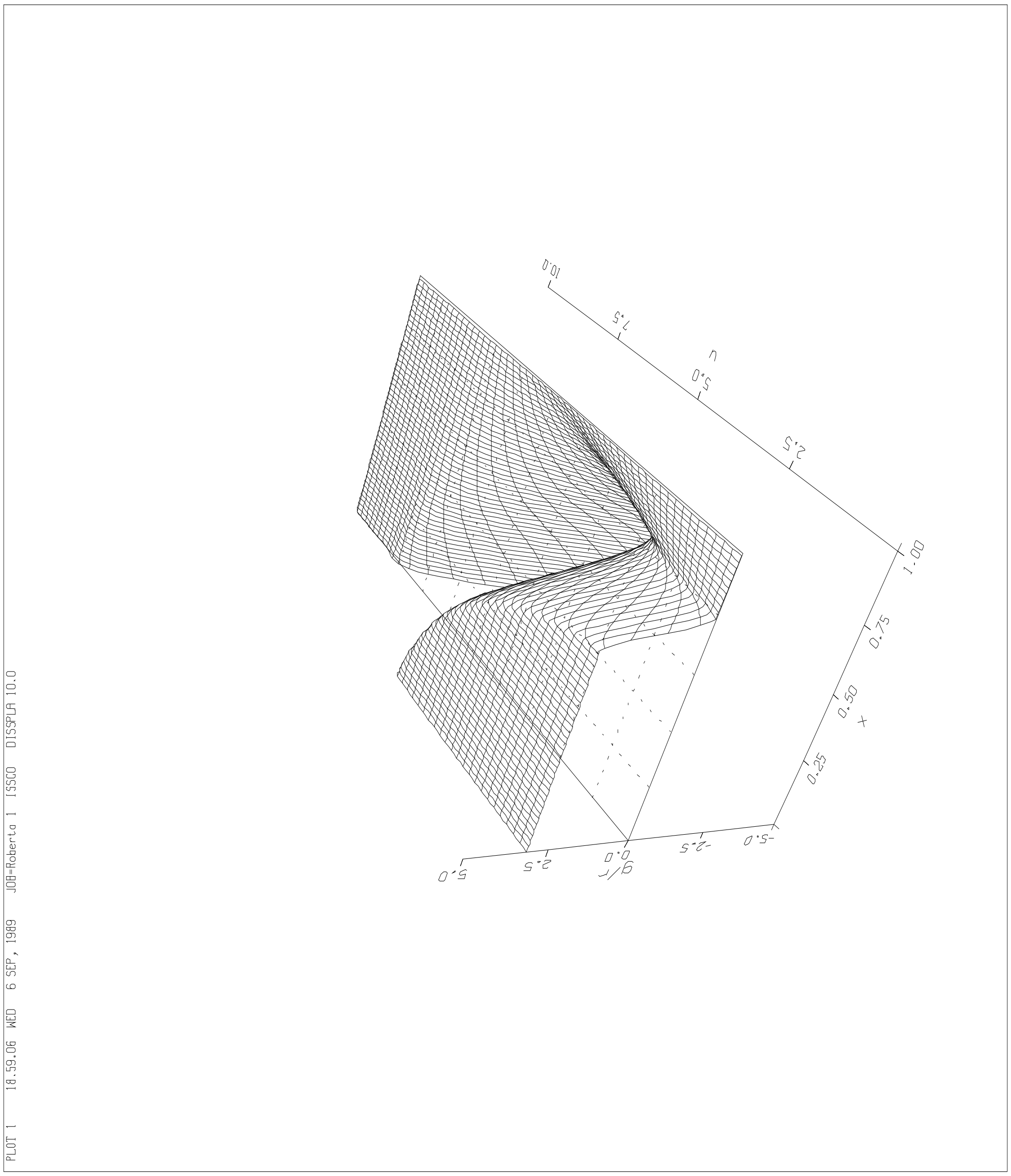

Figure 7: Overview of the evolution of Φ for linear scalar waves. There is no backscattering and the initial field dissipates completely.

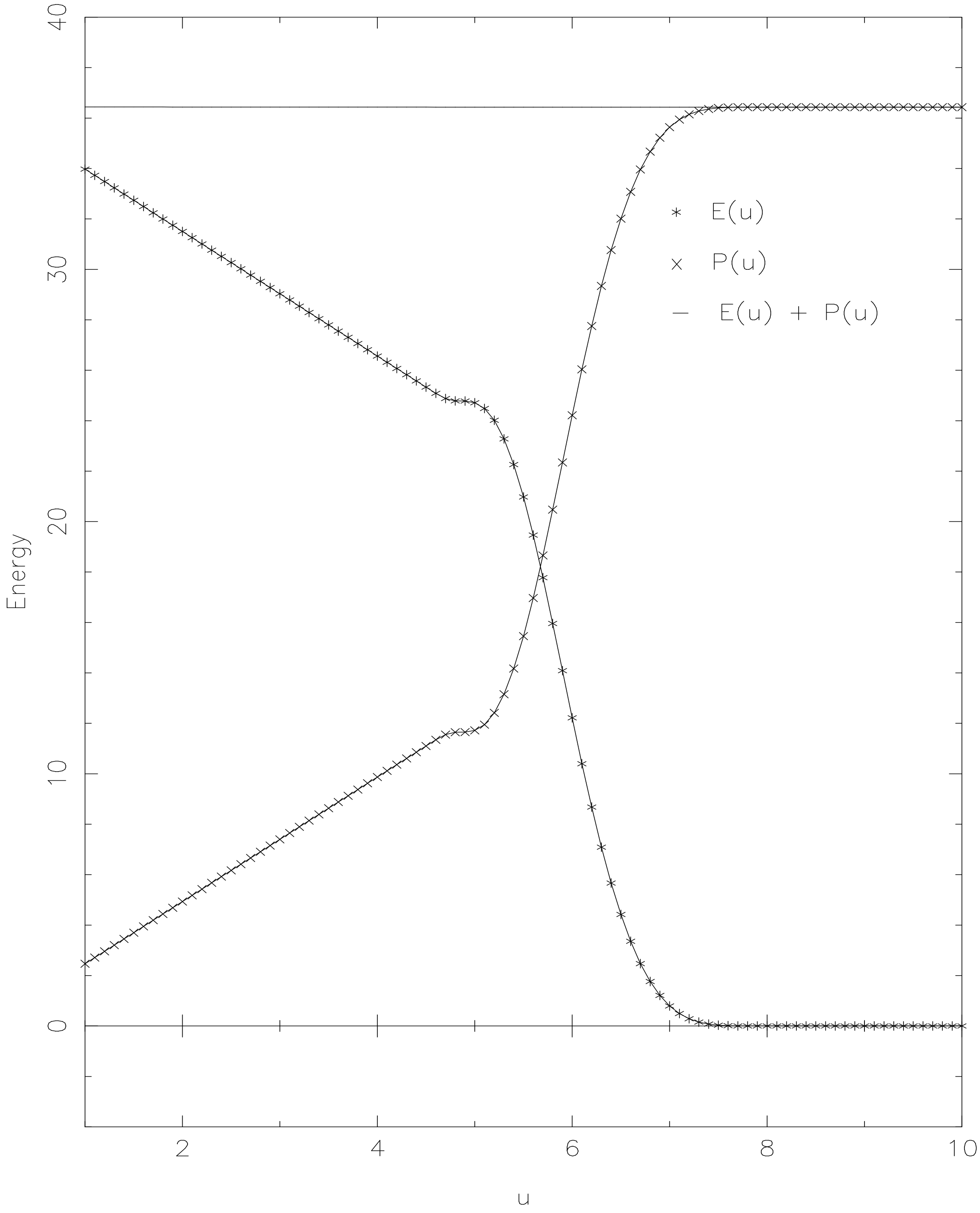

Figure 8: Energy emitted to radiative infinity for linear scalar waves. The graph shows the separate time dependences of the hypersurface energy and the total power radiated at infinity, and verifies the conservation of their sum.

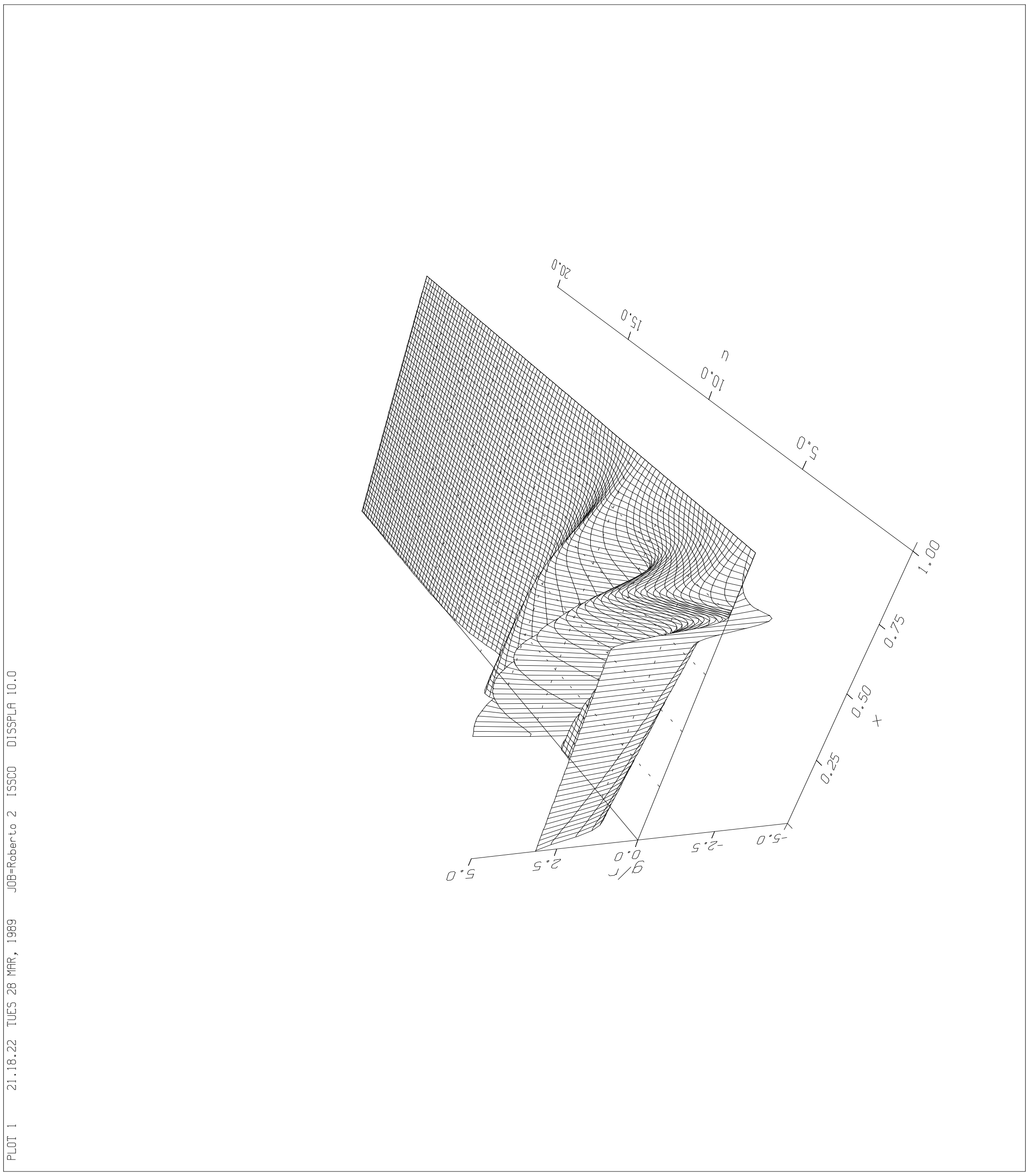

Figure 9: Overview of the evolution of Φ for scalar waves in a Φ^4 potential.

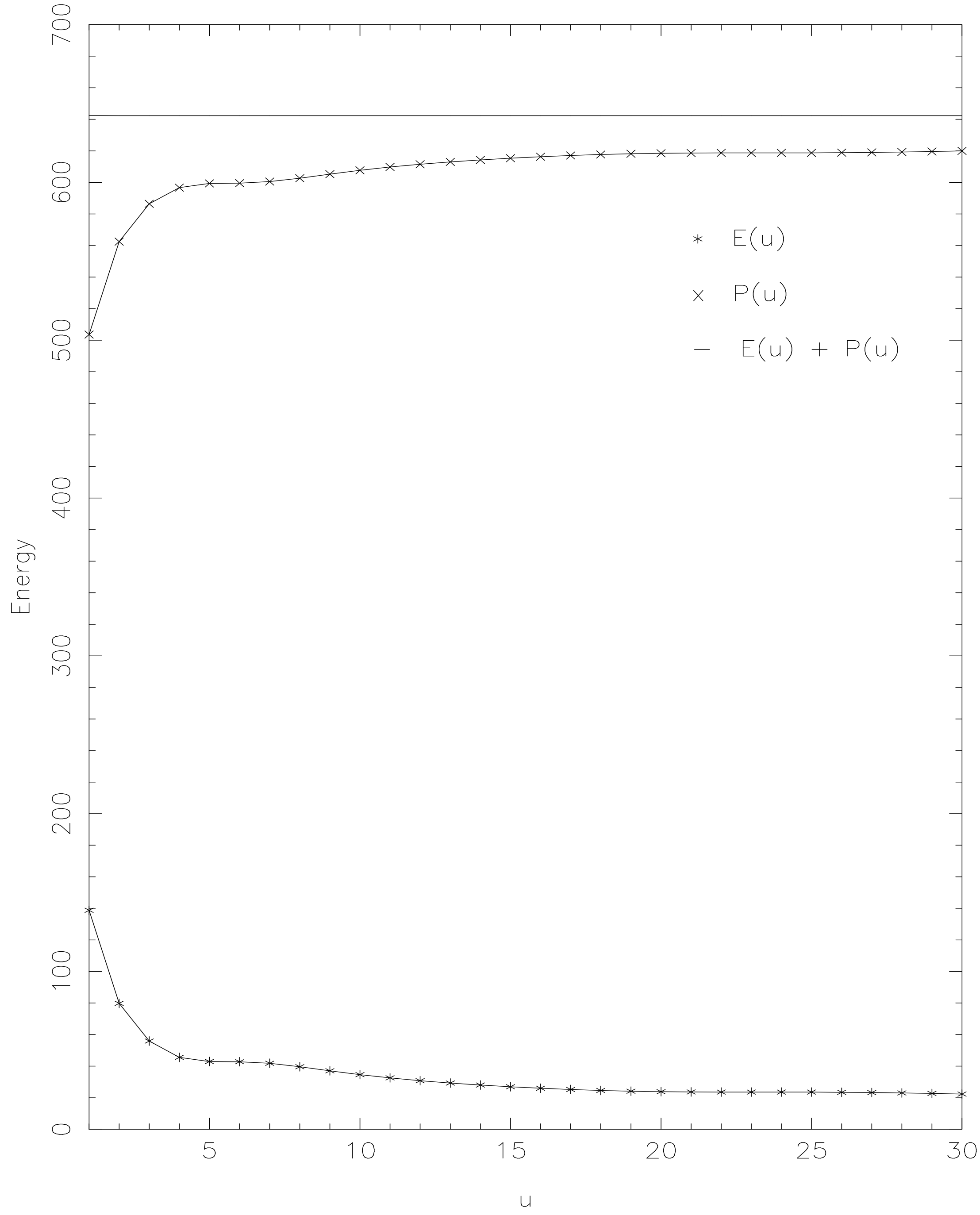

Figure 10: Energy emitted to radiative infinity for scalar waves in a Φ^4 potential. The graph shows the separate time dependences of the hypersurface energy and the total power radiated at infinity, and verifies the conservation of their sum.

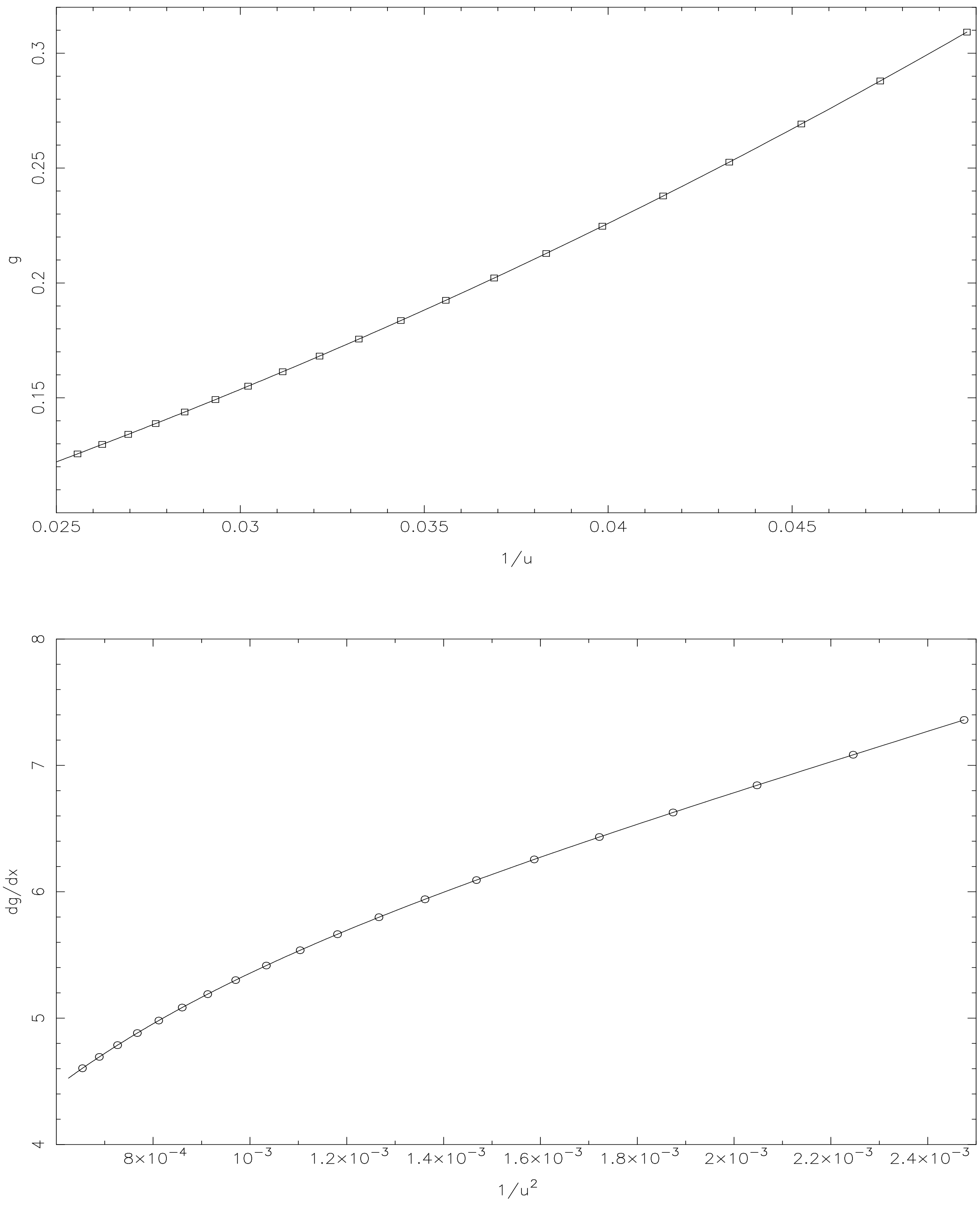

Figure 11: The time dependence of radiative tails for scalar waves propagating in a Φ^4 potential is illustrated by the behavior of g and g_x at radiative infinity.

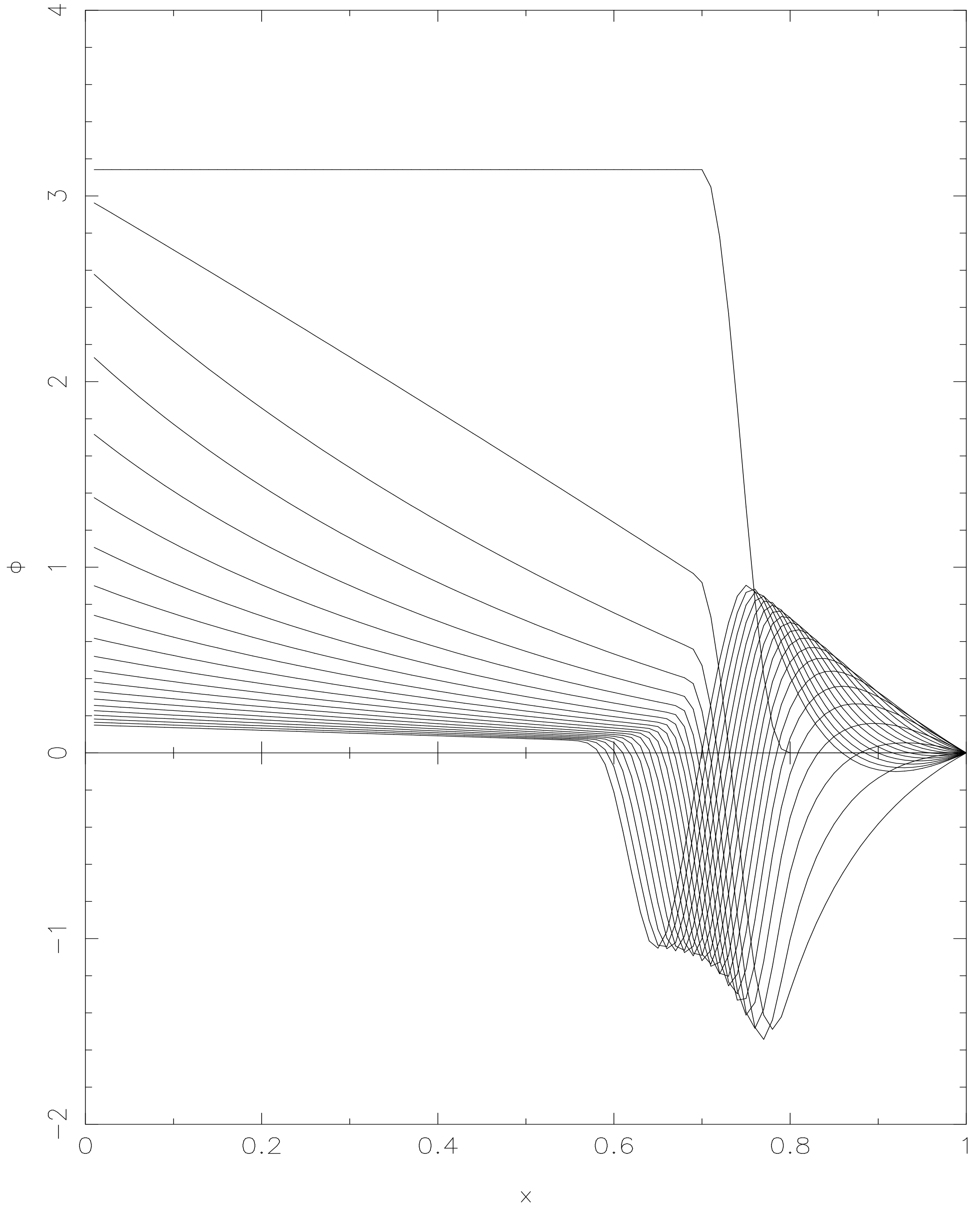

Figure 12: Behavior of constant Φ interior region of initial data for scalar waves propagating in a Φ^4 potential. Note the monotonic approach of the scalar field to zero.

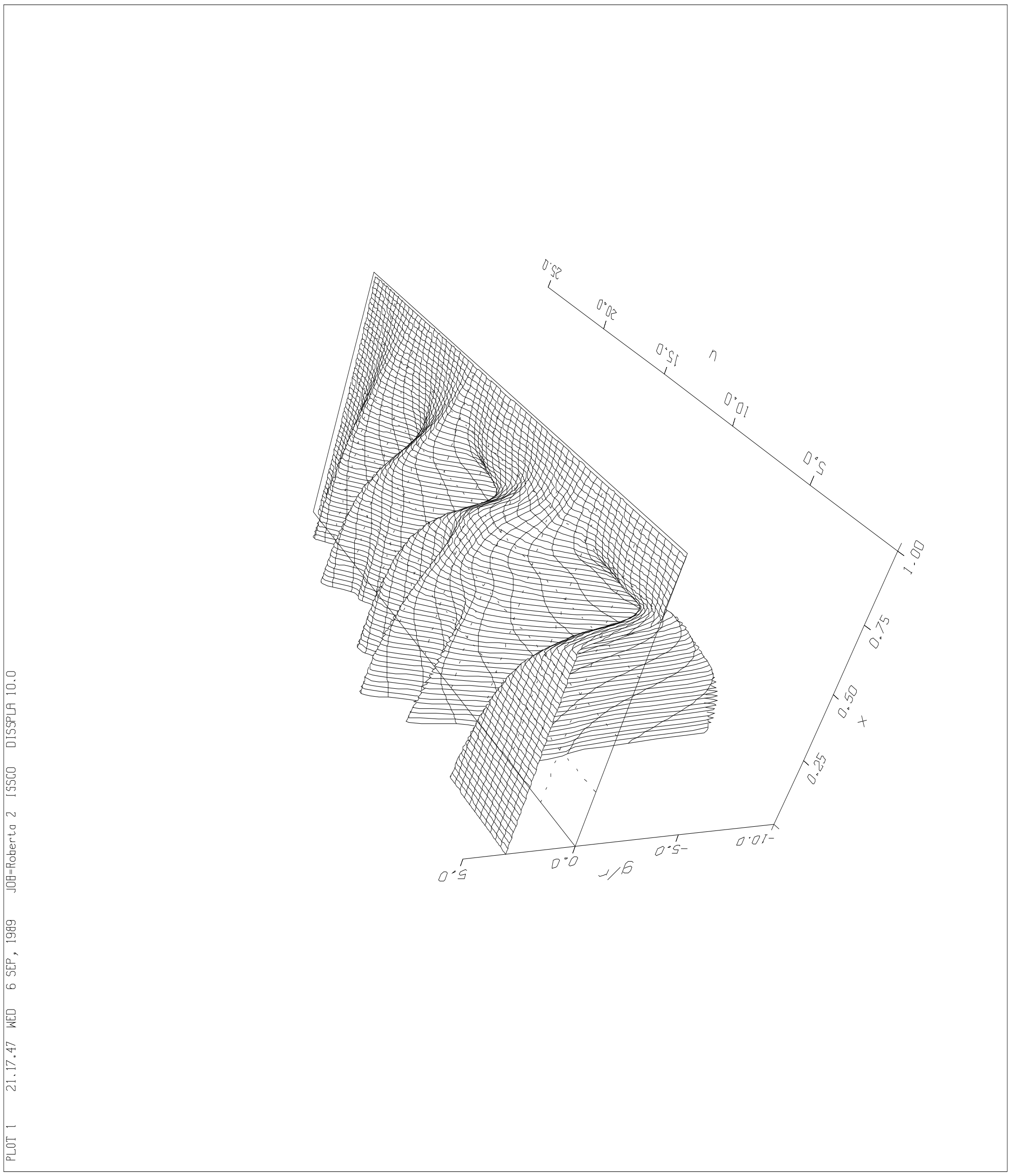

Figure 13: Overview of the evolution of Φ for scalar waves in a $sin^4(\Phi)$ potential. Note the multiple approximate reconstructions of the initial configuration.

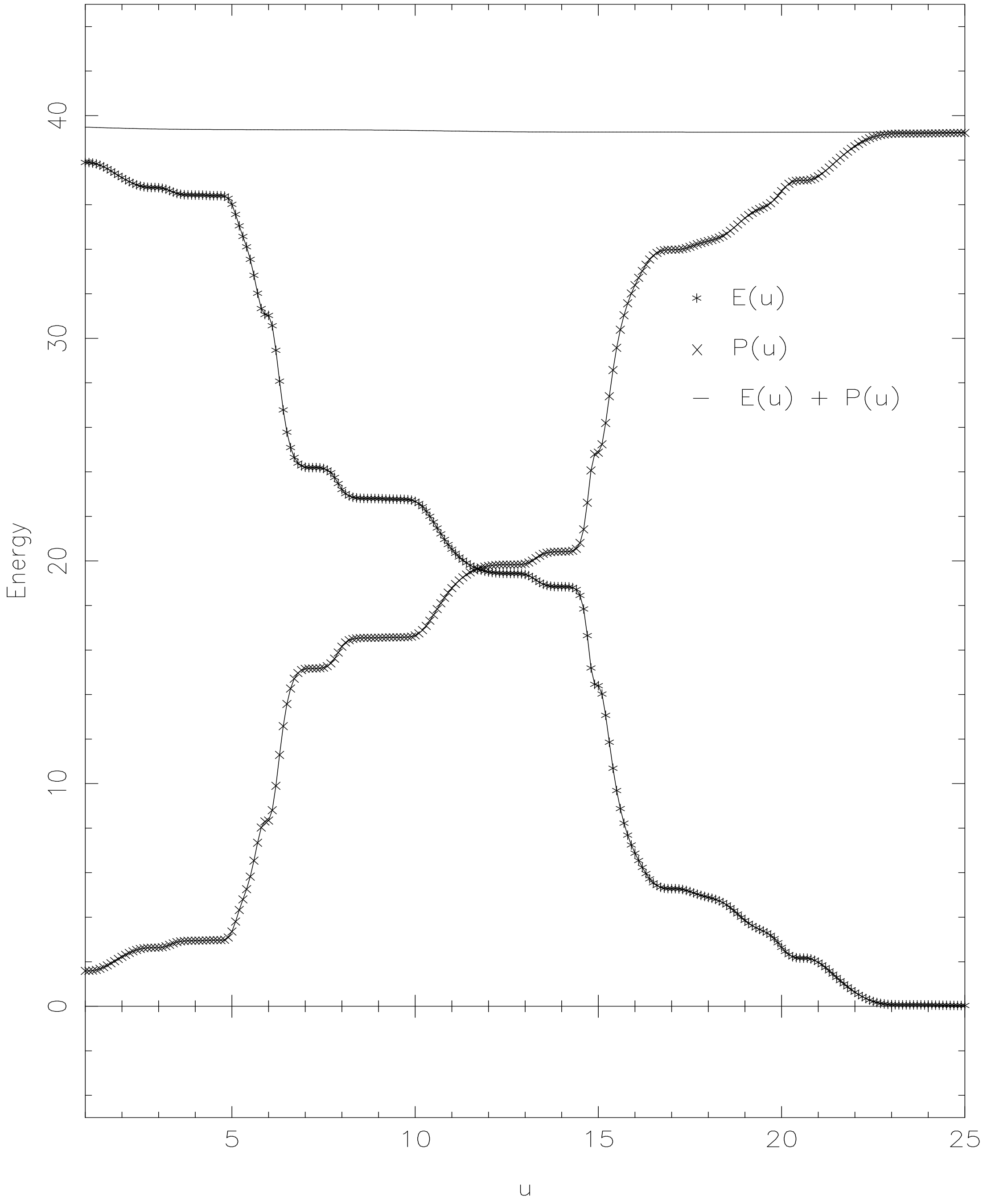

Figure 14: Energy emitted to radiative infinity for scalar waves in a $sin^4(\Phi)$ potential. The graph shows the separate time dependences of the hypersurface energy and the total power radiated at infinity, and verifies the conservation of their sum.

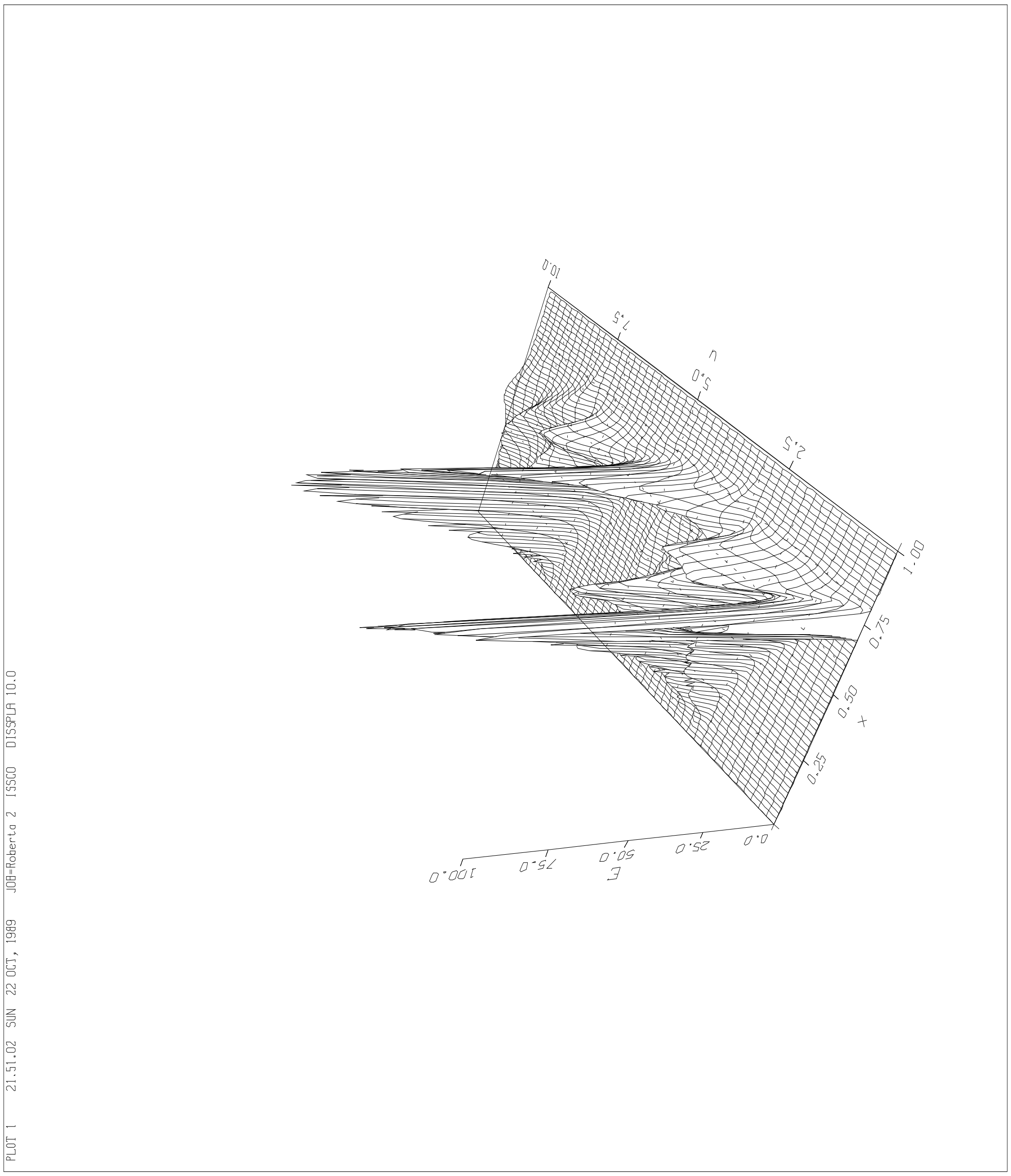

Figure 15: Distribution of energy density for scalar waves propagating in a $sin^4(\Phi)$ potential. Note the approximate reconstruction of the initial state after one crossing time.

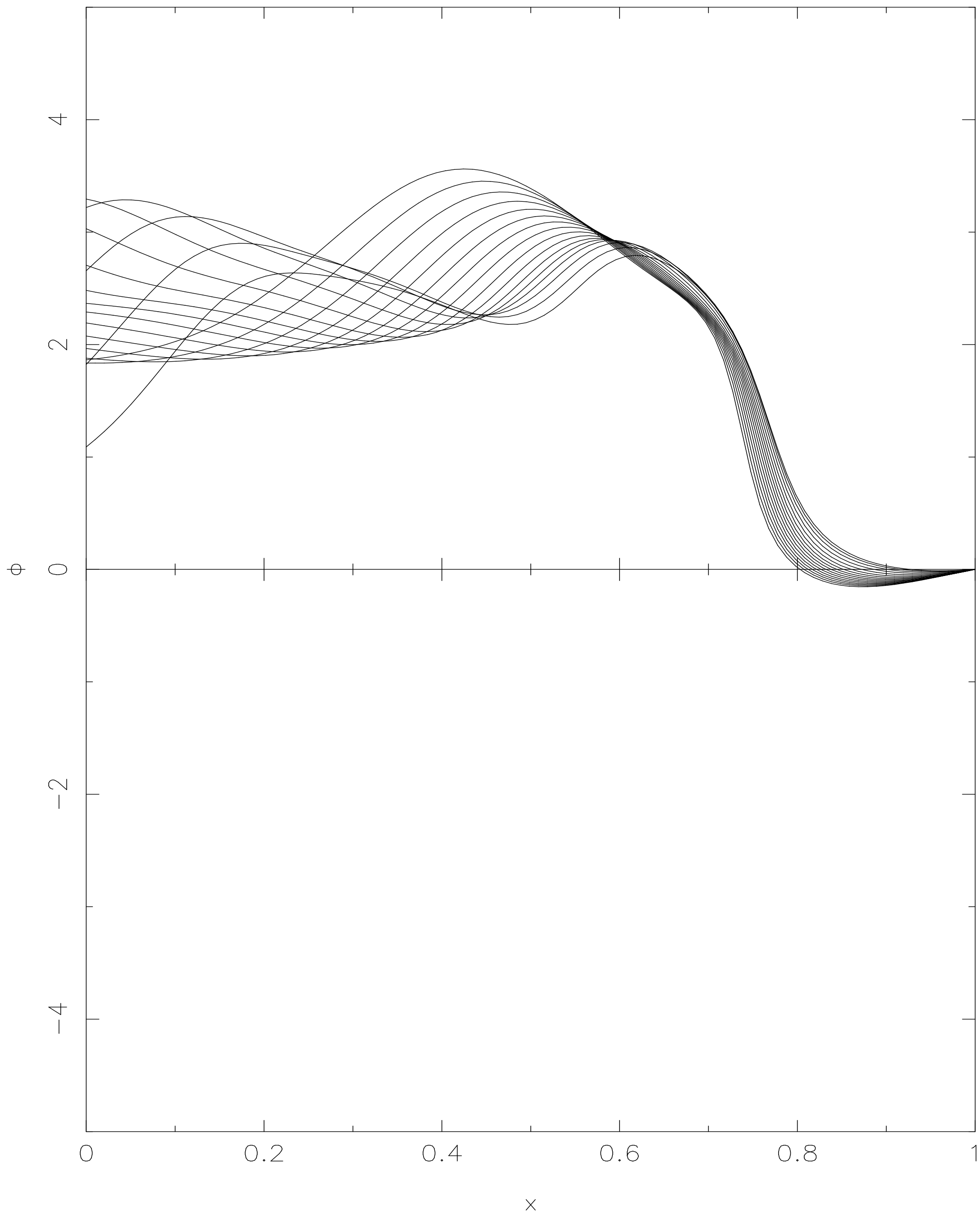

Figure 16: Node formation during the evolution of scalar waves in a $sin^4(\Phi)$ potential. Superimposed curves represent snapshots made between $u = 7.6$ and 9.1 at time intervals $\Delta u = 0.1$.